Heliyon 10 (2024) e26300

Contents lists available at ScienceDirect

Heliyon

journal homepage: www.cell.com/heliyon

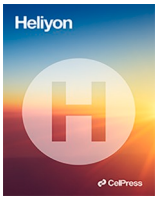

Research article

Transmission efficiency of one tooth difference sine tooth profile planetary reducer

Ying Lu, Lizhong Xu *

School of Mechanical Engineering, Yanshan University, Qinhuangdao, 066004, China

ARTICLE INFO

Keywords:
Sine tooth profile
Planetary reducer
Transmission efficiency
One tooth difference
Friction coefficient

ABSTRACT

The structural size of space exploration and unmanned aerial vehicle manipulator is required to be as small as possible, and the weight must be as light as possible. However, the existing reducers have difficulties in achieving lightweight robot joint drive systems. For it, this paper proposes a single tooth difference continuous sine tooth profile K–H–V type planetary reducer in which pin type equi-speed output mechanism is used. Concerning the reducer, its structural composition and meshing characteristics are analyzed. Based on the findings, the meshing pair's force, the friction coefficient, and the meshing efficiency are investigated. The force and bearing efficiency of the planetary gear are studied, and the efficiency of the equi-speed output mechanism in addition to the total efficiency of the reducer are determined. Moreover, the efficiency of the reducer prototype is measured and compared to the calculated efficiencies. The results show that the gear modulus, the input speed, the surface roughness, and the lubricating oil viscosity have a significant effect on the meshing efficiency. Furthermore, the efficiency of the eccentric bearings is significantly lower than that of the non-eccentric bearings. Therefore, it can be increased by tuning the pressure angle, the tooth number of planetary gear, the tooth height, and the distribution circle radius of the pinhole. In addition, the power loss of the output mechanism has the greatest effect on transmission efficiency. Reducing the center distance, the inner diameter of the rotating arm bearing, and the tooth number of planetary gear, as well as increasing the outer diameter of the pin shaft can reduce the power loss of the output mechanism. The experimental efficiency of the reducer prototype is 82.47%, its computational efficiency is 83.72%, and its error is 1.25%, verifying the correctness of the efficiency calculation method.

1. Introduction

Due to the characteristics of launch, flight, and polar environment work, the structural size of space exploration and unmanned aerial vehicles (UAV) manipulator is required to be as small as possible, and the weight must be as light as possible [1–4]. The University of Illinois in the United States designed a small quad-rotor prototype with a light mechanical arm having two Degrees-Of-Freedom (2-DOF) and carried out its motion control experiments in a two-dimensional plane [5]. Moreover, the University of Sevilla in Spain designed an aerial work robot system, based on UAV, having two 3-DOF robotic arms, and conducted experiments on target detection, attitude estimation, and object grasping during flight [6]. In addition, the Shenyang Institute of Automation, Chinese Academy of Sciences, developed an aerial operation robot with a 5-DOF manipulator and conducted an outdoor flight test [7]. As for

* Corresponding author.
E-mail address: xlz@ysu.edu.cn (L. Xu).

https://doi.org/10.1016/j.heliyon.2024.e26300
Received 17 July 2023; Received in revised form 4 February 2024; Accepted 9 February 2024
Available online 11 February 2024

the Shenzhen Research Institute of Harbin Institute of Technology in China, they studied an 8-rotor aircraft with a 4-DOF manipulator and conducted motion planning experiments based on visual servo [8]. Finally, the state key laboratory of mechanical systems and vibration of Shanghai Jiaotong University in China developed a 6-DOF aerial operation robot, carried out wind turbine blade coating repair experiments, and demonstrated its potential to complete complex aerial operations [9].

Currently, aerial robots are mainly developing through the combination of flight platforms and multi-degree-of-freedom robotic arms, making, therefore, the robot posture more flexible and expanding the range of operation space. However, the operational capability of the aerial robots is limited by the load and mass they can carry. Due to the large proportion of robotic arm mass, its further lightweight becomes the key to ensuring and improving the operational capability of such aerial robots [10–13].

The University of Toulouse in France used carbon fiber to make lightweight robotic arms, which reduced the mass of the robotic arm while ensuring greater stiffness [14]. The University of Sevilla in Spain developed a 4-DOF lightweight flight humanoid robotic arm with dual arms using an aluminum alloy frame structure [15]. Moreover, the Robotics Research Center of Ritsumeikan University in Japan designed a lightweight three-arm flying robot, with each robotic arm having 2-DOF and the arm body made of thin aluminum tubes [16]. In addition, a dual-arm flying robot was jointly developed by Nanyang Polytechnic University in Singapore and the University of Texas in the United States. Each robotic arm had 6-DOF, was made of carbon fiber composite material, and was designed with a gravity center balance mechanism, yielding to an effective reduction of the mass and inertia of the robotic arm [17]. Furthermore, the Royal Airlines Air Robotics Laboratory conducted lightweight design and developed joint drive systems for flight robotic arms using servo actuators with integrated motors, transmissions, and electronic control components produced by Herkulex or Dynamixel Company [18–22].

In summary, the lightweight research of flight robotic arms includes the use of lightweight material for the robotic arm as well as structural lightweight and joint drive system lightweight. In more detail, the lightweight of the joint drive system is mainly achieved by using servo actuators as they have a small size and are lightweight; however, the motion control accuracy and their load-bearing capacity are still low. To improve both factors of the joint drive system of flight robotic arms, the drive scheme of the electric motors, as well as the precision reducers, is considered important development directions [23].

The robot joint drive mainly uses harmonic gear reducers, RV reducers, and planetary gear reducers. The single-stage reduction ratio of the planetary gear reducers is small, requiring multi-step reduction. As a result, the volume and weight of the reducer increase; thus, it is generally used for the joint drive of large robotic arms, such as extravehicular robotic arms of the space station. As for the RV reducers, they have high stiffness and rotational accuracy. However, their structural composition is relatively complex, making it difficult to achieve miniaturization; moreover, it is applied to heavy load situations, such as mounts, arms, and shoulders of the general-size robot [24–26]. Finally, Harmonic reducers have the advantages of a large transmission ratio, small size, and lightweight, and they are mainly used for small arms, wrists, or hands of general-size robots.

At present, robotic arms mainly use small harmonic reducers to achieve lightweight joint drive [27–29]. Under load, the flexible wheel of the small-sized harmonic reducer undergoes significant elastic deformation, decreasing the load-bearing capacity and affecting the positioning accuracy and the dynamic characteristics of the robot's end. Thus, the existing reducers still have difficulties in achieving lightweight robot joint drive systems, which has become a technical bottleneck that restricts the development of further lightweight robotic arms.

For it, various actuators based on functional materials have been developed, including memory alloy actuators [30,31], piezoelectric actuators [32,33], and dielectric elastomer actuators [34], greatly simplifying the driver structure and reducing the driver size. However, this type of driver has relatively small driving capacity and is mainly used in micro robots and micro electromechanical systems.

Therefore, the paper proposes a continuous sine tooth profile reducer. Using the zero-position line of the sine curve as the gear pitch line, one cycle of the curve as the pitch of the sine gear, and the amplitude a of the sine curve as the tooth height of the gear.

The tooth profile of the sine gear reducer is continuous, and the tooth width rapidly decreases from the root to the top of the tooth. It is not easy to interfere when meshing within one tooth difference, making it suitable for single tooth difference planetary gear transmission. This sine profile gear pairs has a relatively small sliding coefficient, low meshing friction loss, and high transmission efficiency. When the gears engage with each other, the entire process is engaged with convex and concave teeth, with low contact stress, and high load-bearing capacity per unit volume. Due to its easy implementation of a single tooth difference structure and large transmission ratio, it is very suitable for lightweight applications in robotic arm drive systems.

Compared to harmonic reducers, the reducers have several advantages such as the large load-bearing capacity, large transmission ratio, the high transmission efficiency, the simple and compact structure, the low meshing impact, and the high stiffness. This makes the reducers avoid decrease of the load-bearing capacity and the rotation accuracy under load. As transmission efficiency is an important factor for evaluating the performance of reducers, this article mainly studies the various power losses and transmission efficiency of this new type of reducer.

In this paper, the single tooth difference continuous sine tooth profile planetary reducer's structural makeup and meshing features are examined. Based on this, the meshing pair's force, the friction coefficient, and the meshing efficiency are studied. Meanwhile, the force and the bearing efficiency of the planetary gear are investigated, and the efficiency of the equi-speed output mechanism plus the total efficiency of the reducer are determined. The efficiency of the reducer prototype is measured and compared to the calculated efficiencies, verifying the correctness of the efficiency calculation method.

The paper includes six parts: (1) structure and meshing characteristic equation of the new reducer; (2) meshing force and meshing efficiency of sine gear pairs; (3) forces and bearing efficiency on planetary gears; (4) other power losses and overall efficiency of the reducer; (5) results and discussion; (6) conclusion.

2. Structure and meshing characteristics

The continuous sine one tooth difference planetary gear reducer consists mainly of a pair of internal and external sine tooth profile gears with one tooth difference and an equi-speed output mechanism (see Fig. 1), mainly composed of the following three parts:

(1) Input part: it contains rolling bearings on the input shaft and its eccentric shaft supports the planetary gear;
(2) Transmission part: it consists of a central wheel and a planetary wheel. The planetary gear is installed on the rolling bearing on an eccentric shaft and meshed with the sinusoidal tooth profile of the central wheel;
(3) Equi-speed output part: it includes evenly distributed pin holes on the planetary gears, the pin shafts, the pin sleeves, the discs, and the cross-roller bearings. The pin shafts are fixed on the disc, and the pin sleeve can rotate on the pin shafts.

When the sinusoidal one-tooth difference reducer operates, the motor is connected to the input shaft, and the eccentric shaft section of the input shaft drives the planetary gear to rotate and engages with the central wheel. Moreover, when the eccentric axis rotates, the planetary gear rotates around the eccentric axis while rotating itself. The planetary gear moves one tooth distance relative to the center wheel while it rotates one circle. Thus, a power with a large reduction ratio is obtained and it is delivered by the cross roller bearing of the equi-speed output part.

Using the zero-position line of the sine curve as the gear pitch line, one cycle of the curve as the pitch of the sine gear, and the amplitude a of the sine curve as the tooth height of the gear. In the Cartesian coordinate system, the equation of any point on the sine tooth profile is expressed as follows [35]:

$$\begin{cases} x_1 = \left(a\cos(z_1\varphi) + \sqrt{{r_1}^2 - a^2\sin^2(z_1\varphi)}\right)\sin\varphi \\ y_1 = \left(a\cos(z_1\varphi) + \sqrt{{r_1}^2 - a^2\sin^2(z_1\varphi)}\right)\cos\varphi \end{cases} \tag{1}$$

where a is the tooth height coefficient, z_1 represents the tooth number of the planet gear, φ indicates the position coordinate of any point on the sine tooth profile, and r_1 is the radius of the pitch circle of the planet gear.

According to the meshing principle and under the condition of internal meshing, in the Cartesian coordinate system, the equation of the tooth profile curve of the internal gear 2 meshing with gear 1 is expressed as follows [35]:

$$\begin{cases} x_2 = x_1\cos(\varphi_1\text{-}\varphi_2)\text{-}y_1\sin(\varphi_1\text{-}\varphi_2) + a_0\sin\varphi_2 \\ y_2 = x_1\sin(\varphi_1\text{-}\varphi_2) + y_1\cos(\varphi_1\text{-}\varphi_2) + a_0\cos\varphi_2 \end{cases} \tag{2}$$

where a_0 is the center distance, φ_1 is the rotating angle of the planet gear, φ_2 is the rotating angle of the center ring; moreover, $\varphi_2 = \varphi_1/i$, $i = z_2/z_1$, that is the speed ratio of the fixed shaft transmission between the two gears. In addition, z_2 is the tooth number of the central ring.

According to the principle of gear meshing, the tooth profile, presented in Eq. (1), is substituted into the meshing equation to obtain the relative velocity vector as follows [36]:

$$\vec{v}_{12} = [\omega_2(y_1 + a_0\cos\varphi_1) - \omega_1 y_1]\vec{i}_1 + [\omega_1 x_1 - \omega_2(a_0\sin\varphi_1 + x_1)]\vec{j}_1 \tag{3}$$

where ω_1 and ω_2 are the angular speeds of the planetary gear and the center ring, respectively.

From Eq. (3), the relative velocity components in the directions x and y could be given by:

$$\begin{cases} v_{12}^x = \omega_2(y_1 + a_0\cos\varphi_1) - \omega_1 y_1 \\ v_{12}^y = \omega_1 x_1 - \omega_2(a_0\sin\varphi_1 + x_1) \end{cases} \tag{4}$$

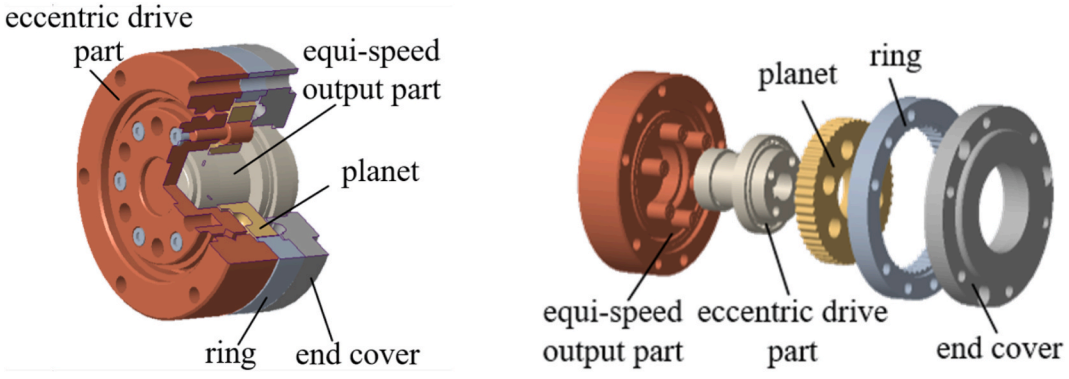

Fig. 1. Sinusoidal one tooth difference planet reducer.

According to the definition of the entrainment speed that is equal to the average value of the speed of a pair of gears, the entrainment speed vector U_{12} of the central wheel and planetary gear can be obtained as follows [36]:

$$\overrightarrow{U_{12}} = \frac{1}{2}\left[(\omega_1 x_1 + \omega_2(x_1 + a_0 \sin\varphi_1))\overrightarrow{j}_1 - (\omega_1 y_1 + \omega_2(y_1 + a_0\cos\varphi_1))\overrightarrow{i}_1\right] \tag{5}$$

Moreover, the curvature is defined as the rate of rotation of the tangent direction of a point on the curve relative to the arc length. According to differential geometry, the equation modelling the curve curvature is [36]:

$$\mathrm{K} = \frac{\mathrm{x}'\mathrm{y}'' - \mathrm{x}''\mathrm{y}'}{(\mathrm{x}'^2 + \mathrm{y}'^2)^{\frac{3}{2}}} \tag{6}$$

where x' and y' are the first derivative of the sine tooth profile position x and y versus the tooth profile angle φ, respectively. Furthermore, x'' and y'' represent the second derivatives of the sine tooth profile position x and y versus the tooth profile angle φ, respectively.

Therefore, substituting Eq. (1) into (6) generates the curvature K_1 of the sinusoidal tooth profile 1. Its mathematical equation is as follows:

$$K_1 = -\frac{A \quad B + a \quad b^2 \quad {z_1}^2 \quad D}{A\sqrt{B \quad C - b^2 \quad (2 \quad a^2 - {r_1}^2) + 3 \quad a^2 \quad b^2 \quad D^2 + a^4 \quad E^2 \quad ({z_1}^2 - 1) \quad (D^2 - E^2) + a^2 \quad b^2 \quad {z_1}^2 E^2}} \tag{7}$$

where $A = ({z_k}^2 - 1)\ a^2\ \sin(\ z_k\varphi_2)^2 + b^2$, $B = \sqrt{{r_1}^2 - a^2\ \sin(z_1\varphi)^2}$, $D = \cos(z_1\varphi)$, $E = \sin(\ z_1\varphi)$, and $C = 2\ a\ {r_1}^2\ \cos(\ z_1\varphi) - 2\ a^3\ \cos(\ z_1\varphi)\sin^2(\ z_1\varphi) + 2\ a^3\ {z_1}^2\ \cos(\ z_1\varphi)\sin^2(\ z_1\varphi)$.

Similarly, by substituting Eq. (2) into (6), the curvature K_2 of the conjugate tooth profile can also be obtained.

The pressure angle is the key parameter to evaluate the transmission performance of the reducer. This gear angle is the acute angle between the speed v and the force F (see Fig. 2) where o_1 and o_2 are the centers of gears 1 and 2, respectively.

Assume that the slope of the straight line along the velocity v direction is k_v, the slope of the straight line along the normal force F direction is k_n, the pressure angle α_{k1} of the meshing point is expressed as follows (see Fig. 2):

$$\alpha_{k1} = atan\left|\frac{k_n - k_v}{1 + k_n k_v}\right| \tag{8}$$

Moreover, the meshing point K represents any point on the tooth profile c_1 of gear 1. The coordinates of K in the coordinate system $\Sigma_1(x_1, o_1, y_1)$ are (x_{k1}, y_{k1}). Thus, the slope of the straight line k_v along the velocity v direction is as follows:

$$k_v = -\frac{x_{k1}}{y_{k1}} \tag{9}$$

Furthermore, the slope of the straight line along the normal force F direction is as follows:

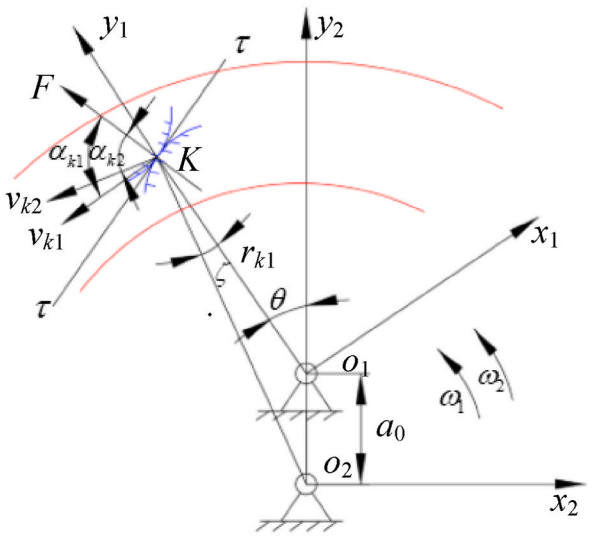

Fig. 2. Pressure angles of the internal meshing sine gear pair.

$$k_n = -\frac{dx_{k1}}{dy_{k1}} \tag{10}$$

Substituting Eqs. (8) and (9) into (10), the slope of the straight line along the normal force F direction can be determined. In addition, the coordinates of the point K in the coordinate system $\Sigma_2(x_2, o_2, y_2)$ are (x_{k2}, y_{k2}). Thus,

$$r_{k1} = a\cos(z_1\varphi) + \sqrt{r_1^2 - a^2\sin(z_1\varphi)} \tag{11}$$

$$r_{k2} = \sqrt{x_{k2}^2 + y_{k2}^2} \tag{12}$$

Considering ζ the angle between lines o_1K and o_2K, then:

$$\zeta = a\cos\left[\left(r_{k1}^2 + r_{k2}^2 - a_0^2\right) / 2r_{k1}r_{k2}\right] \tag{13}$$

Referring to Fig. 2, the pressure angle α_{k2} of gear 2 at meshing point K is determined as follows:

$$\alpha_{k2} = \alpha_{k1} - \zeta \tag{14}$$

Substituting Eqs. (11)–(13) into (14), the pressure angle α_{k2} can be determined.

3. Forces on meshing pair and meshing efficiency

Fig. 3 presents a force model of a sine tooth profile gear where F_{ni} is the normal force applied to any tooth. Thus, the normal force W, per unit length, can be calculated as follows:

$$W = \frac{F_{ni}}{L} \tag{15}$$

where L represents the length of the contact line.

According to the torque balance conditions of the multi-tooth meshing, one can write:

$$T_2 = \Sigma^{z_s}{}_{i=1} F_{ni}\cos\alpha_i r_i \tag{16}$$

where T_2 is the load torque, z_s presents the tooth number in mesh, α_i indicates the pressure angle of the tooth i, and r_i is the distance between the meshing point of the tooth i and the circle center.

According to the deformation coordination conditions, the equation to calculate the force on any pair of teeth is defined as follows:

$$F_{ni} = F_0\cos\alpha_i \tag{17}$$

where F_0 is the maximum common divisor of forces applied to the teeth under multi-tooth meshing.

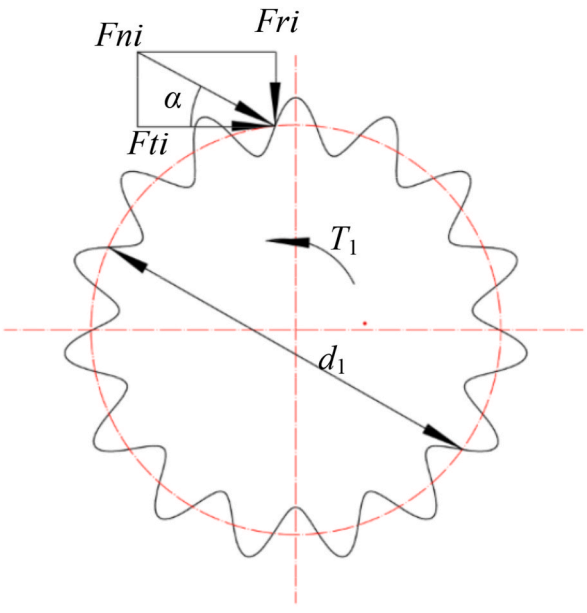

Fig. 3. Forces on the sine gear tooth.

Substituting Eq. (17) into (16) yields in the following:

$$F_0 = \frac{T_2}{\sum^{z_s}_{i=1} \cos^2 \alpha_i r_i} \tag{18}$$

Moreover, by substituting Eq. (18) into (17), the normal force F_{ni} can be obtained:

$$F_{ni} = \frac{T_2 \cos \alpha_i}{\sum^{z_s}_{i=1} \cos^2 \alpha_i r_i} \tag{19}$$

Finally, by substituting Eq. (19) into (15), the normal force W, per unit length, when the central wheel and the planetary gear mesh can be obtained as follows:

$$W = \frac{T_2 \cos \alpha}{L \sum^{z_s}_{i=1} \cos^2 \alpha_i r_i} \tag{20}$$

When both gears mesh each other, due to the speeds at the contact point of the two gears that are different, the relative sliding between these gears occurs which causes the relative sliding friction loss between the tooth surfaces. The equation modelling the sliding friction power loss of meshing pair of the sine gear reducer is expressed as follows:

$$P_s = f_s \cdot F_{ni} \cdot v_{12} \times 10^{-3} \tag{21}$$

where P_s is the sliding friction power loss, f_s represents the sliding friction coefficient, and v_{12} indicates the relative sliding speed at the meshing point of the two gears.

Gear meshing friction power loss includes rolling friction and sliding friction power loss. Studies show that the rolling friction power loss is much smaller than sliding friction power loss. Due to space limitations, only the sliding friction power loss is considered here.

Currently, there have been many theoretical and experimental studies regarding the friction coefficient of the gear tooth surfaces. The commonly used friction coefficient calculation methods have certain limitations in practical uses. Therefore, this paper compares two friction coefficient calculation models and selects a model suitable for the sine gear meshing.

(1) Benedict & Kelley model

The friction coefficient can be calculated as follows [37]:

$$f_s = 0.0127 \lg \left| \frac{29.66 \times 10^9 W}{\eta_0 v U^2} \right| \tag{22}$$

where η_0 is the dynamic viscosity of the lubricating oil, here the normal force W per unit length can be calculated by Eq. (20).

(2) EHL model

The friction coefficient can be calculated as follows [38]:

$$f_s = e^{f\left(SR, P_h, \eta_0, S_{avg}\right)} P_h^{b2} |SR|^{b3} U^{b7} \eta_0^{b7} R^{b8} \tag{23}$$

where $f(SR, P_h, \eta_0, S_{R_a})$ can be obtained from the below equation:

$$f(SR, P_h, \eta_0, S_{R_a}) = b_1 + b_4 |SR| P_h \log_{10}(\eta_0) + b_5 e^{-|SR| p_h \log_{10}(\eta_0)} + b_9 e^{R_a} \tag{24}$$

where P_h is the contact stress (expressed in Hertz), $P_h = \sqrt{\frac{F_{ni}}{\pi L} \cdot \frac{\frac{1}{\rho_1} - \frac{1}{\rho_2}}{\frac{1-\mu_1^2}{E_1} + \frac{1-\mu_2^2}{E_2}}} = \sqrt{\frac{W \cdot E}{2\pi R}}$, and E is the equivalent elastic modulus of the two gears; moreover, SR is the slip roll ratio of the two contact tooth surfaces and it is expressed as follows: $SR = v_{12}/U_{12}$ (v_{12} and U_{12} can be calculated by Eqs. (4) and (5)). As for R_a, it represents the surface roughness factor, R is the equivalent curvature radius in meshing point of the two gears, it equal to reciprocal of comprehensive curvature (see Eq. (7)), e indicates the exponential function, and, finally, b_1,b_2, …,b_9 are the coefficients (refer to Table 1). Eqs. (4), (19) and (22) or (23) plus (24) are substituted into (21), the sliding friction power loss of meshing pair of the sine gear reducer can be determined.

Based on the above analysis of the frictional power loss of the meshing pair of sine gear reducers, the meshing efficiency η of the sine gear reducer can be determined as follows:

Table 1
b_i parameter values for friction coefficient calculation.

b_i	b_1	b_2	b_3	b_4	b_5	b_6	b_7	b_8	b_9
values	8.916	1.033	1.036	−0.354	2.812	−0.101	0.752	−0.391	0.620

$$\eta = \frac{P - P_s}{P} \times 100\% \tag{25}$$

where P represents the input power.

Substituting Eq. (21) into (25), the meshing efficiency η of the sine gear reducer can be determined.

4. Forces on the planet gear and bearing efficiency

In the sine gear reducer, the forces applied to the planet gear are shown in Fig. 4. Here, F_n is the normal force applied from the center ring, Q_i is the force from the pin i ($i = 1, 2,.., n$, n being the pin number), and F_{R1} is the force from rolling bearing on the eccentric shaft. Thus, the total force F_{R1} from the pins can be given as follows:

$$\sum Q_i = \left(\sum_{i=1}^{n} Q_i\right)_m = \frac{4T_2}{\pi R_\omega} \tag{26}$$

where R_ω is the radius of the pinhole center circle.

Referring to Fig. 4, the force F_{R1} from the rolling bearing can be calculated as follows:

$$F_{R1} = \sqrt{F_{ti}^2 + \left[F_{ri} + \left(\sum Q_i\right)_m\right]^2} \tag{27}$$

Moreover, the total force F_{R1} can be expressed as the product of a coefficient δ and the force F_3. Here, F_3 is the force from the rolling bearing when the eccentric is absent. Thus,

$$F_{R1} = \delta \cdot F_3 \tag{28}$$

where $F_3 = \sqrt{F_{ri}^2 + F_{ti}^2} = F_{ni}$ and δ is called the load proportion coefficient of the bearing on the eccentric shaft.

From Eqs. (27) and (28), it could be known:

$$\delta = \frac{\sqrt{F_{ti}^2 + \left[F_{ri} + (\sum Q_i)_m\right]^2}}{F_{ni}} \tag{29}$$

Substituting Eqs. (26) and (27) into (29) yields in:

$$\delta = \sqrt{1 + \frac{8 \sin\alpha_i \psi \sum_{i=1}^{z} \cos^2\alpha_i}{\pi \cos\alpha_i} + \frac{16\psi^2 \sum_{i=1}^{z} \cos^4\alpha_i}{\pi^2 \cos^2\alpha_i}} \tag{30}$$

where

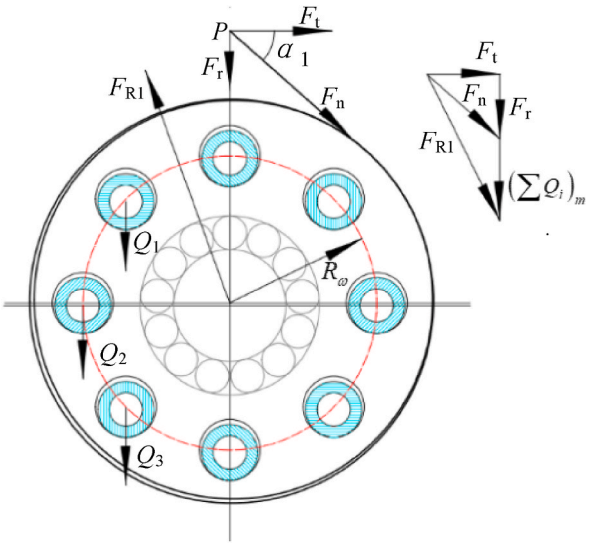

Fig. 4. Forces applied to the planet gear.

$$\psi = \frac{r_i}{R_\omega} = \frac{r_1}{R_\omega}\left[\frac{a}{r_1}\cos(z_1\varphi) + \sqrt{1 - \left(\frac{a}{r_1}\right)^2 \sin^2(z_1\varphi)}\right] \tag{31}$$

Furthermore, the planetary gear is mounted on the eccentric shaft through a rolling bearing. During the transmission process, due to the eccentricity effect, the friction power loss increases compared to the ordinary bearings. The friction power loss of the rolling bearing on the eccentric shaft is equal to:

$$P_b = 2\pi r_p f n_1 \cdot F_{R1} \tag{32}$$

where r_p is the inner radius of the eccentric rotating rolling bearing, f is the friction coefficient of the rolling bearing, and n_1 is the speed of the eccentric shaft.

Thus, the bearing efficiency on the eccentric shaft is expressed as follows:

$$\eta_r = 1 - \frac{P_b}{P} = 1 - \frac{r_p f \cdot F_{R1}}{T_1} \tag{33}$$

where the input power $P = 2\pi n_1 T_1$, T_1 is the input torque, P_b is determined by Eq. (32).

The friction power loss P_1 of the rolling bearing on the non-eccentric shaft section is expressed as follows:

$$P_1 = 1.05 \times 10^{-4} n_1 M_f \tag{34}$$

where M_f represents the friction torque of the rolling bearing on the non-eccentric shaft section.

In addition, the bearing efficiency on the non-eccentric shaft section is equal to:

$$\eta_b' = \frac{P - P_1}{P} \tag{35}$$

where P_1 is determined by Eq. (34).

Based on Eqs. (33) and (35), the total rolling bearing efficiency of the reducer can be given by:

$$\eta_b = \eta_r \cdot \eta_b' \tag{36}$$

5. Other power loss and reducer efficiency

In the equi-speed output mechanism, the sliding friction power loss occurs between the pins and pin sleeves. When the input eccentric shaft rotates one turn, the sliding curve length of the pin sleeve across the pin is equal to:

$$\mathrm{Ls} = 2\pi(2\mathrm{r_x} + 2\mathrm{a_0})\text{-}2\pi(2\mathrm{r_x}) = 4\pi\mathrm{a_0} \tag{37}$$

where r_x is the radius of the pin.

From Eq. (37), the relative sliding velocity between the pin and pin sleeve is represented as follows:

$$v_s = L_s n_1/60 = \pi a_0\, n_1/15 \tag{38}$$

From Eq. (38), the sliding friction power loss in the equi-speed output mechanism can be given by:

$$P_K = \left(\sum_{i=1}^{n} Q_i\right)_m f_K v_s = \frac{\pi n_1 a_0 f_K}{15}\left(\sum_{i=1}^{n} Q_i\right)_m \tag{39}$$

where f_k represents the friction coefficient between the pin and its sleeve.

From Eq. (39), the efficiency of the equi-speed output mechanism can be modelled as follows:

$$\eta_K = 1 - \frac{P_K}{2\pi n_1 T_1} = 1 - \frac{2 f_K a_0 i_{12}}{15\pi R_\omega} \tag{40}$$

The power loss related to the load in the reducer includes the meshing power loss, the bearing power loss, and the power loss in the equi-speed output mechanism; the corresponding efficiency is expressed as follows:

$$\eta_l = \eta \cdot \eta_b \cdot \eta_K \tag{41}$$

Substituting Eqs. (25), (36) and (40) into (41), the efficiency related to the load can be determined.

Other power losses, P_0, include oil agitation and splashing loss, as well as seal friction loss, and it is not related to the load; it can be calculated using the below equation [39].

$$P_0 = 10^{-7} a_0 (n_1/60)^{\frac{4}{3}\left(\frac{750}{n_1}\right)^{0.1}} (\gamma_{50} + 90) \tag{42}$$

where γ_{50} is the viscosity of lubricating oil.

Thus, the transmission efficiency of the sinusoidal planetary reducer, having one tooth difference, can be calculated by:

$$\eta_H = \frac{\eta_1(P - P_0)}{P} = \eta_1\left(1 - \frac{P_0}{P}\right) \tag{43}$$

As for the input power, it is expressed as follows:

$$P = \frac{T_2 \pi n_1}{30 i_{12} \eta_H} \tag{44}$$

Substituting Eq. (44) into (43) yields in:

$$\eta_H = \frac{\eta_1}{1 + K_n \frac{P_0}{T_2} \eta_1} \tag{45}$$

where $K_n = 30i_{12}/n_1\pi$ and i_{12} is the speed ratio of the reducer (it is equal to $i_{12} = z_1/(z_1\text{-}z_2)$).

Substituting Eqs. (41) and (42) into (45), the transmission efficiency of the sinusoidal planetary reducer can be determined.

6. Results and discussion

6.1. Friction coefficient

Using Eqs. (22) and (23), the friction coefficients, expressed as the function of the meshing position angles, are calculated (refer to Fig. 5a). The parameters of the example reducer are shown in Table 2. Other parameters are given in Table 3. Referring to Fig. 5a, one can identify the following:

(1) the Benedict & Kelley model shows that the friction coefficients increase first with the meshing position angle, reach the maximum at the pitch point, and then decrease with the meshing position angle. The friction coefficient is the minimum at the top and root of the teeth;
(2) the EHL model shows that the friction coefficients decrease first with the meshing position angle, gets to zero at the pitch point, and then increase with the meshing position angle. The friction coefficient value is the minimum at the pitch point; Substituting Eqs. (22) and (23) into (21), the friction power loss, considered as the function of the meshing position angles, are given (see Fig. 5b). Therefore, Fig. 5b shows:
(1) the Benedict & Kelley model shows that the sliding friction power loss of the sine tooth profile reducer presents a parabolic shape, which first increases and then decreases, and the maximum sliding friction power loss occurs at the pitch point;
(2) the EHL model shows that the sliding friction power loss of the sine tooth profile reducer increases first and then decreases with the meshing position angle. The sliding friction power loss is zero at the tooth root and the pitch point, and it is the maximum at a 1/4 position angle. Referring to the pitch point to the tooth top, the sliding friction power loss first increases and then decreases with the meshing position angle again. The sliding friction power loss is zero at the tooth top, and it is the maximum at a 3/4 position angle again.

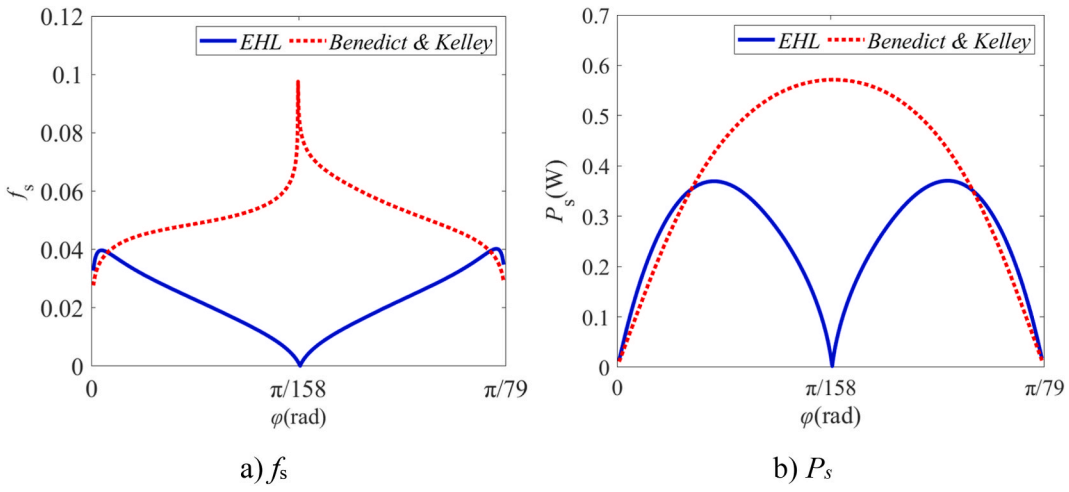

Fig. 5. Friction coefficient and friction power loss.

Table 2
Parameters of sine tooth profile reducer.

i_{12}	a/mm	a_0/mm	z_1	z_2	m/mm	L/mm	E_1/Pa	E_2/Pa	μ_1	μ_2
79	0.4	0.45	79	80	0.9	8	2.12×10^{11}	2.12×10^{11}	0.28	0.28

Table 3
Other parameters.

n_1/rpm	T_1/N·mm	η_0/MPa·s	R_a/μm
300	400	2×10^{-8}	0.4

Moreover, the sliding friction coefficient, calculated by Benedict & Kelley model, has a sharp point at the pitch point. This is due to the relative sliding speed at the zero point where the calculated friction coefficient has a sudden change and tends to infinity, which is inconsistent with the real situation.

However, the friction coefficient and friction power loss, calculated by the EHL model, are zero at the pitch point, which is consistent with the real situation; thus, the EHL model is used to calculate the friction coefficient and the sliding friction power loss in this paper.

6.2. Meshing efficiency

Using Eqs. (23)–(27), changes in the meshing efficiency with the related parameters are investigated (see Fig. 6). When one parameter is altered, the other parameters of the reducer are constant (see Tables 2 and 3). Therefore, Fig. 6 shows:

(1) The meshing efficiency of the sine tooth reducer varies periodically with the meshing position angle, and the period is determined by the number z_1 of planetary gear teeth, as it is equal toπ/z_1. This is determined by the periodicity of the friction coefficient and the force acting on the meshing pair. As for the meshing efficiency of the sine tooth reducer, it has the highest value near the pitch point, the tooth root, and the tooth top, with a maximum value of 99.37% whereas it has the lowest value at the one-quarter and three-quarter tooth profile angles, with a minimum value of 96.58%. The average meshing efficiency is 97.96%;
(2) When the gear modulus m changes, without varying the period of change in the meshing efficiency concerning the meshing position angle, the meshing efficiency at the pitch point, the tooth root, and the tooth top remains unchanged. The meshing efficiency at other points increases with the modulus m. The meshing efficiency changes significantly with modulus m near one-quarter and three-quarters tooth profile angles. This is due to the increase of the module m that causes the relative sliding friction coefficient of the gear to decrease, resulting in the decrease of friction power loss (see Fig. 6a);
(3) When the tooth height coefficient changes, the variation period of the meshing efficiency remains constant as well as the meshing efficiency at the pitch point, the tooth root, and the tooth top. The meshing efficiency of other points slightly decreases with the increase of tooth height coefficient a. This is mainly due to the increase of tooth height coefficient a that rises the relative sliding speed, which grows sliding friction coefficient and friction power loss (see Fig. 6b);
(4) When the number of planetary gear teeth z_1 changes, the meshing efficiency period changes as well. As the number of planetary gear teeth increases, the period decreases. Meanwhile, the meshing efficiency increases with the number of teeth. This is due to the increase of the number of planetary gear teeth z_1, resulting in the reduction of the relative sliding speed, which reduces the sliding friction coefficient and the sliding friction power loss (see Fig. 6c);
(5) When the input speed n_1 changes, the variation period of meshing efficiency remains constant. Moreover, the meshing efficiency of each point decreases with the increase of the input speed n_1. The reduction in the meshing efficiency at the tooth top, the pitch point, and the tooth root is not obvious. The reduction in the meshing efficiency is due to the increase of the input speed n_1 that leads to the increase of the sliding friction power loss (see Fig. 6d);
(6) When the surface roughness R_a changes, the meshing efficiency at the pitch point, the tooth root, and the tooth top also remain constant. The meshing efficiency of the other points decreases with the increase of surface roughness R_a. This is due to the increase of surface roughness R_a that leads to the increase of sliding friction coefficient and the increase of sliding friction power loss (see Fig. 6e);
(7) When the lubricating oil dynamic viscosity η_0 changes, the meshing efficiency at the pitch point, the tooth root, and the tooth top remains unchanged. The meshing efficiency of the other points decreases with the increase of the lubricating oil η_0 dynamic viscosity. This is due to the dynamic viscosity increase causing the rise of the sliding friction coefficient and the sliding friction power loss (see Fig. 6f).

To sum up, increasing the modulus m and the tooth number z_1, or reducing the tooth height coefficient a, the surface roughness R_a, the input speed n_1, and the lubricating oil dynamic viscosity η_0 could increase the meshing efficiency of the sine tooth profile reducer. Among them, m, n_1, R_a, and η_0 have significant effects on the meshing efficiency, while a and z_1 have a smaller impact on the meshing efficiency.

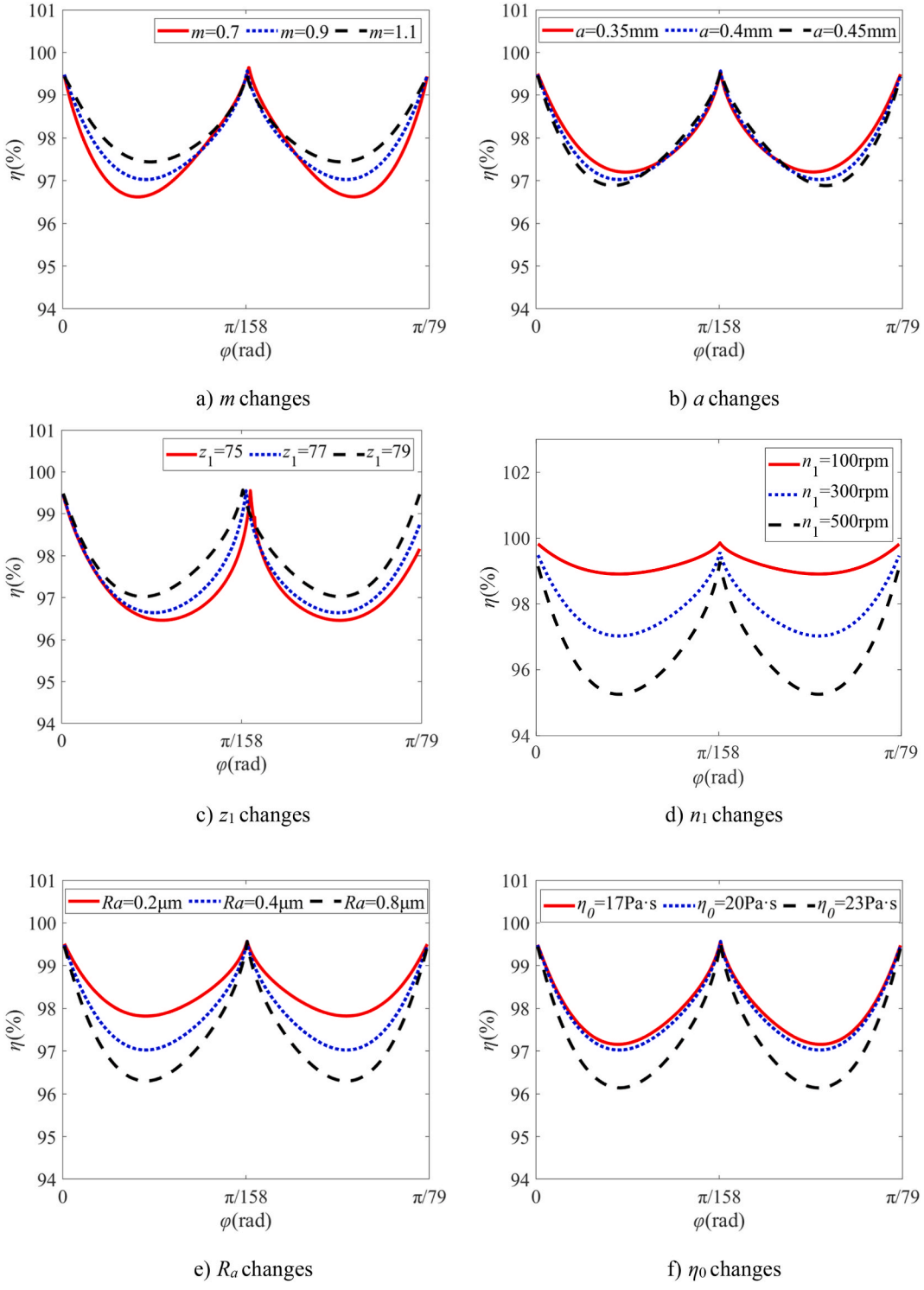

Fig. 6. Changes in meshing efficiency with related parameters.

6.3. Bearing efficiency

Referring to Eqs. (30) and (31), the load proportion coefficient δ of the bearing on the eccentric shaft is related to the pressure angle α_1, tooth number z_1, and the ratios a/r_1 and r_1/R_ω. Using both listed equations, the load proportion coefficient δ as the function of these

parameters is investigated (see Fig. 7). When one parameter changes, the other parameters of the reducer remain constant (refer to Tables 2 and 3). Moreover, the parameters of the bearings are shown in Table 4. As for the results, Fig. 7 shows the following:

(1)When the pressure angle α_1 of the sine gear changes from 10° to 70°, the load proportion coefficient δ increases. When the pressure angle α_1 is smaller than 50°, the δ increases slowly with α_1. However, when α_1 is above 50°, δ increases rapidly. When α_1 is at 10° and 50°, the load proportion coefficient difference of the bearing is 1.62 times and when α_1 is at 50° and 70°, the load proportion coefficient difference of the bearing is 1.58 times. Therefore, to reduce δ, α_1 of the sine gear should have a small value (see Fig. 7a);

(2) When the planet tooth number z_1 of the sine reducer changes from 39 to 79 (here, $\alpha_1 = 20°$), the load proportion coefficient δ increases. This means that a smaller value of z_1 could cause a decrease in δ (see Fig. 7b);
(3) When the ratio a/r_1 changes from 0.01 to 0.04 ($\alpha_1 = 20°$, constant), the load proportion coefficient δ increases with the ratio a/r_1. So, decreasing the ratio a/r_1 could reduce the value of δ. Therefore, when the radius r_1 of the planet gear is given, decreasing the tooth height coefficient a could decrease the load proportion coefficient δ (see Fig. 7c).
(4) When the ratio r_1/R_ω changes from 1.2 to 1.6 (also $\alpha_1 = 20°$), the load proportion coefficient δ increases. So, decreasing the ratio r_1/R_ω could reduce the value of δ. When the radius r_1 of the planet gear is given, increasing the radius R_ω of the pinhole circle would decrease δ (see Fig. 7d).

To sum up, reducing the pressure angle α_1, the tooth number z_1, and the ratios a/r_1 and r_1/R_ω could decrease the load proportion coefficient δ. Among them, α_1 has the greatest effect on the value of δ.

Using Eq. (36), the efficiency of the eccentric bearing of the reducer is calculated (refer to Fig. 8). When one parameter changes, the other parameters of the reducer are constant (see Tables 2 and 3). Moreover, the parameters of the bearings are shown in Table 4. Referring to Fig. 8, one can conclude the following:

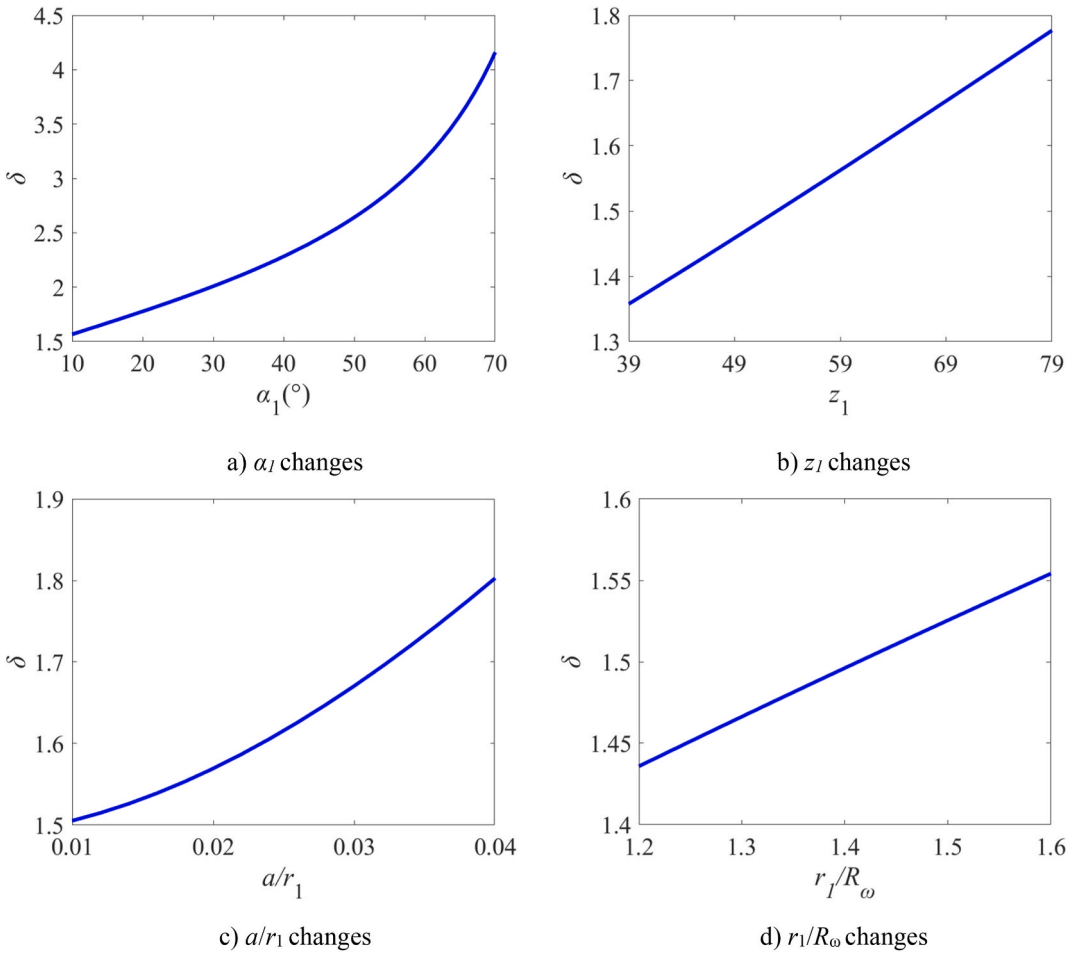

Fig. 7. Changes of load proportion coefficient δ of the bearing with parameters.

Table 4
Parameters of bearings.

R_ω/mm	r_p/mm	r_x/mm	f	f_k
26.2	10	6	0.001	0.03

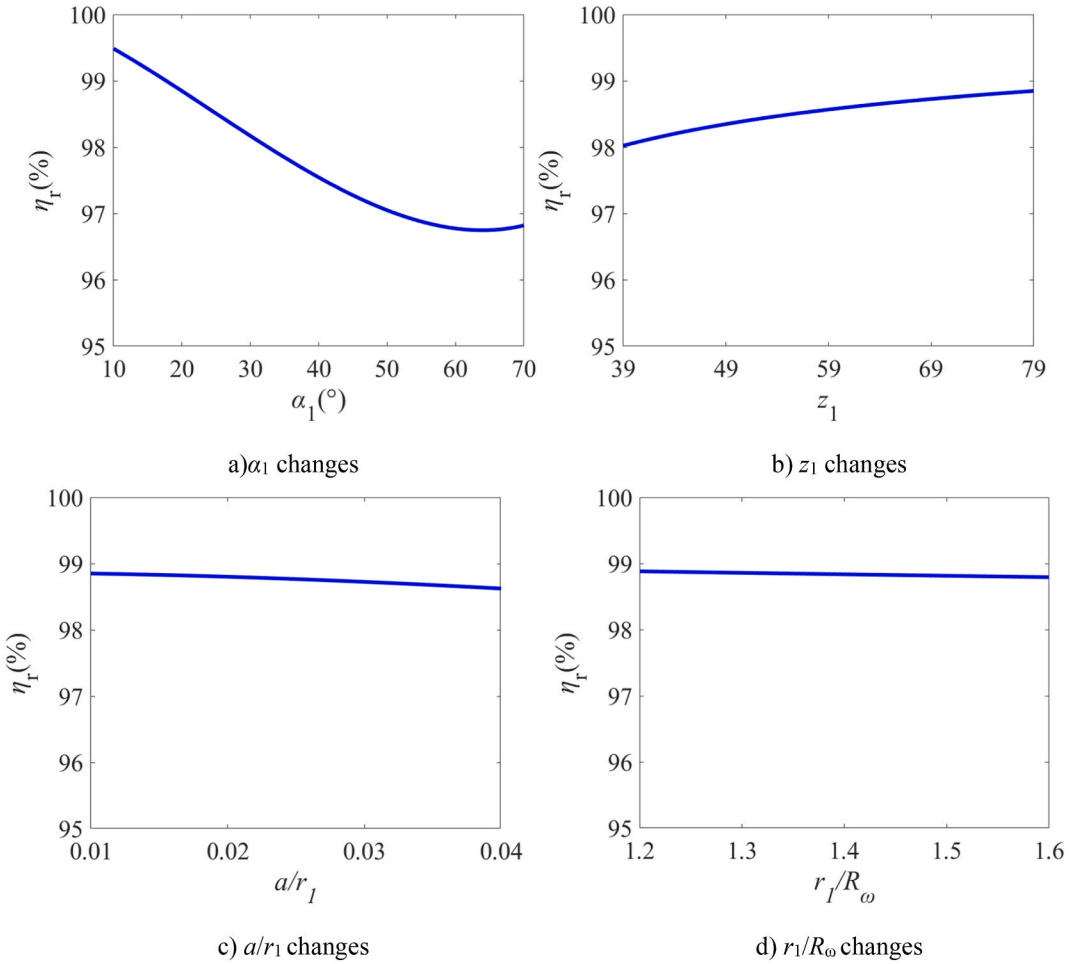

Fig. 8. Changes of efficiency η_r of the bearing on an eccentric shaft with parameters.

(1) The efficiency η_r of the eccentric bearing decreases with increasing the pressure angle α_1. It is because the load proportion coefficient δ of the bearing increases with α_1. It should be noted that the normal force F_3 decreases while α_1 increases for pressure angles above 50°. This may yield in the decrease of the efficiency η_r with the pressure angle as it becomes slower and the efficiency η_r begins to increase with the pressure angle when this latter is above 65°(see Fig. 8a);
(2) Although the load proportion coefficient of the eccentric bearing increases with the tooth number z_1 of the planetary gear, the efficiency η_r increase as well with z_1. It is due to the normal force F_3 that decreases when z_1 increases. In this case, the normal force F_3 has a greater effect on the efficiency η_r of the eccentric bearing than the load proportion coefficient δ (see Fig. 8b);
(3) The efficiency η_r decreases while the ratio a/r_1 or r_1/R_ω increases. It is because the load proportion coefficient δ of the eccentric bearing increases with the ratio a/r_1 or r_1/R_ω. When the radius r_1 of the planet gear is constant, decreasing the tooth height coefficient a or increasing the radius R_ω of the pinhole circle could decrease the value of δ to increase the efficiency η_r (see Fig. 8c and d).

To sum up, to increase the efficiency η_r of the eccentric bearing, the pressure angle α_1 and the ratio a/r_1 or r_1/R_ω should have small values whereas the tooth number z_1 of the planet should have a large value. Here, the pressure angle α_1 is the most effective control parameter of the efficiency η_r of the eccentric bearing.

Referring to Eq. (36), the total bearing efficiency of the reducer is investigated (see Fig. 9). In this case, η_{b1} is the bearing efficiency

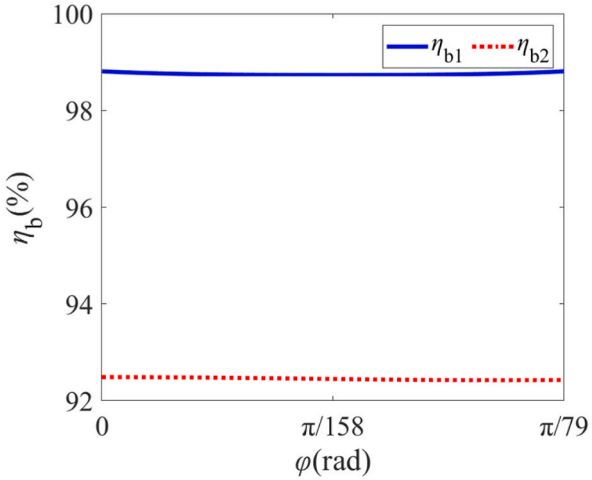

Fig. 9. Bearing efficiencies with and without eccentricity.

without eccentricity (here, $a = 0.4$ mm, $z_1 = 79$, $r_1 = 35.55$ mm, and $R_\omega = 26.2$ mm), and η_{b2} is the bearing efficiency with eccentricity (where $a = 0.5$ mm, $z_1 = 39$, $r_1 = 35.55$ mm, and $R_\omega = 22.22$ mm). The results show that the bearing efficiency with eccentricity is about 92.58% whereas the bearing efficiency without eccentricity is about 98.73%. The difference between both bearing efficiencies is about 6.15%. Therefore, it is necessary to choose relevant parameters reasonably in the design of the eccentric bearing of the reducer to avoid large bearing friction power loss in the eccentric shaft.

6.4. Total efficiency of reducer

Based on the parameters given in Table 2, a model machine of the sine tooth profile reducer is produced (see Fig. 10a). Using the efficiency testing platform shown in Fig. 10b and c, the transmission efficiency of this model machine is measured. The efficiency

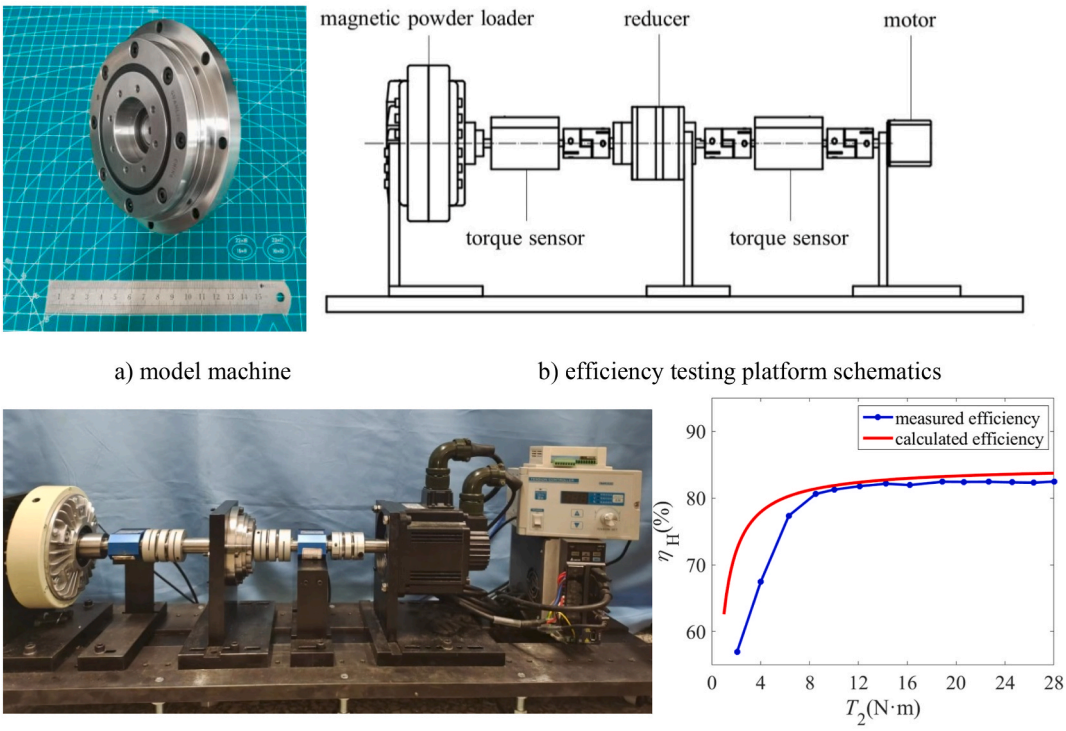

Fig. 10. Testing platform and comparison of calculative and testing efficiencies.

testing platform mainly includes: motor, coupling, torque sensor, tested reducer, and loading device (see Fig. 10b and c). The range of the input torque sensor is 10 Nm, with an accuracy of 0.1%. The output end torque sensor has a range of 100 Nm and an accuracy of 0.2%. It can be used for the measurement of torque at the output and input ends, and based on this, the transmission efficiency of the reducer can be determined.

The input speed n_1 is taken to be 500 rpm whereas $\gamma_{50} = 400$ mm^2/s. The comparison between the measured and calculative efficiencies is given in Fig. 10d. The findings can yield in the following conclusions:

(1) When the load torque T_2 is below 10 Nm, the transmission efficiency of the reducer increases rapidly with T_2. However, when T_2 is above 10 Nm, the transmission efficiency of the reducer increases slowly with T_2. Finally, when the load torque is equal to 28 Nm, the transmission efficiency of the reducer reaches 82.47%;
(2) The calculated and the experimental efficiency changes along with the load torque are basically the same. However, there are still some differences, and the calculated efficiency under low load is relatively high. When the torque is above 10 Nm, there is a better consistency between the calculated and the experimental efficiencies. Meanwhile, when the output torque is 28 Nm, the calculated efficiency is 83.72% whereas the measured efficiency is 82.47%, with a difference of 1.25%.
(3) The reducer efficiency is 83.72%, and the total power loss is 16.28%. In this case, the meshing power loss is 3.55%, the bearing friction power loss is 2.27%, the power loss in the equi-speed output mechanism is 8.61%, and the oil agitation and splashing loss is 1.85%. This implies that the power loss in the equi-speed output mechanism has the greatest effect on the reducer efficiency.

Therefore, in the design of the sine reducer, to ensure high efficiency, special attention should be paid to reducing the power loss of the output mechanism.

7. Conclusions

In this paper, a sine one-tooth difference planetary reducer is proposed. The meshing pair forces, the friction coefficient, the meshing efficiency, the forces on the planetary gear, the bearing efficiency, the efficiency of the equi-speed output mechanism and the total reducer efficiency are investigated. A reducer prototype is produced and its efficiency is measured and compared to the calculative one. The results show the following:

(1) The meshing efficiency of the reducer varies periodically with the meshing position angle. It can be improved by increasing the modulus and the tooth number of the gear while reducing the tooth height coefficient, the surface roughness, and the lubricating oil dynamic viscosity.
(2) The bearing efficiency difference with and without the eccentricity could reach 6.15%. To reduce the power loss of the eccentric bearing, the pressure angle, the tooth number of planetary gear, the tooth height coefficient, the planetary gear radius, and the distribution circle radius of the pinhole should be reasonably selected.
(3) The reducer meshing power loss is 3.55%, the bearing friction power loss is 2.27%, the power loss in the equi-speed output mechanism is 8.61%, and the oil agitation and splashing loss is 1.85%. These results confirm that the power loss in the equi-speed output mechanism has the greatest effect on the reducer efficiency.
(4) The calculated maximum efficiency is 83.72%, and the measured maximum efficiency is 82.47%, with an error of 1.25%. This result verifies the correctness of the calculation method. The measured efficiency of 82.47% is higher than 65–72% of harmonic gear reducers.

In the reducer, the flexible ring is removed. Thus, the friction power loss from the flexible ring deformation is avoided and the meshing efficiency is increased. Therefore, it is more suitable for lightweight applications of robot robotic arm drive systems.

The efficiency calculation equation here is only applicable to situations where good oil film lubrication is achieved. In the future, a different friction coefficient calculation model should be used to calculate the reducer efficiency under other friction state, and some influencing factors and their effects on splashing loss and seal friction power loss should be considered.

CRediT authorship contribution statement

Ying Lu: Investigation, Methodology, Software, Writing – original draft. **Lizhong Xu:** Conceptualization, Investigation, Methodology, Supervision, Writing – review & editing.

Declaration of competing interest

The authors declare that they have no known competing financial interests or personal relationships that could have appeared to influence the work reported in this paper.

Nomenclature

DOF Degrees-Of-Freedom

RV reducers rotating vector reducers
UAV Unmanned Aerial Vehicles
a is the tooth height coefficient
a_0 is the center distance
b_1,b_2, …,b_9 are the coefficients related to friction coefficient
e is the base of the exponential function
E is the equivalent elastic modulus of the two gears
E_1 and E_2 is the elastic modulus of gear 1 and gear 2 materials, respectively
f is the friction coefficient of the rolling bearing
f_k is the friction coefficient between the pin and its sleeve
f_s is the sliding friction coefficient between two gears
f (SR,P_h, η_0, S_{Ra}) is the intermediate function to determine friction coefficient
F is the normal force applied to sine tooth profile
F_{ni} is the normal force applied to any tooth of the sine gear
F_{ri} is the radial force applied to any tooth of the sine gear
F_{ti} is the tangent force applied to any tooth of the sine gear
F_0 is the maximum common divisor of forces applied to the teeth under multi-tooth meshing
F_3 is the force from the rolling bearing without eccentricity
F_{R1} is the force from rolling bearing on the eccentric shaft
F_n is the total normal force applied to the planet gear
F_r is the total radial force applied to the planet gear
F_t is the total tangent force applied to the planet gear
i is the speed ratio of the fixed shaft transmission between the two gears, $i = z_2/z_1$
i_{12} is the speed ratio of the reducer, $i_{12} = z_1/(z_1\text{-}z_2)$
k_v is the slope of the straight line along the velocity direction
k_n is the slope of the straight line along the normal force direction
K is the curvature of the tooth profile
K_1 is the curvature of the sinusoidal tooth profile 1
K_2 is the curvature of the tooth profile 2
K_n is a coefficient, $K_n = 30i_{12}/n_1\pi$
L is the length of the contact line, it is equal to the thickness of the gear
L_s is the sliding curve length of the pin sleeve across the pin
m is the gear module
M_f is the friction torque of the rolling bearing on the non-eccentric shaft section
n_1 is the speed of the eccentric input shaft
P is the input power
P_0 is the power losses, not related to the load
P_1 is the friction power loss of the rolling bearing on the non-eccentric shaft section
P_b is the friction power loss of the rolling bearing on the eccentric shaft
P_s is the sliding friction power loss between two gears
P_h is the contact stress between two gears
Q_i is the force from the pin i (i = 1, 2,.., n, n being the pin number)
r_1 is the radius of the pitch circle of the planet gear
r_p is the inner radius of the eccentric rotating rolling bearing
r_x is the radius of the pin
r_{k1} is the position coordinate of any point on the sine tooth profile in pole coordinate system
R is the equivalent curvature radius in meshing point of the two gears
R_a is the tooth surface roughness of the gear
R_ω is the radius of the pinhole center circle
SR is the slip roll ratio of the two contact tooth surfaces, $SR = v_{12}/U_{12}$
T_1 is the input torque
T_2 is the load torque
U_{12} is the entrainment speed at the meshing point between two gears
v_{12} is the relative sliding speed at the meshing point of the two gears
v_s is the relative sliding velocity between the pin and pin sleeve
$\vec{v}_{12}$ is the relative sliding velocity vector between two gears
v_{12}^x is the component of the relative sliding velocity between two gears in the x axis
v_{12}^y is the component of the relative sliding velocity between two gears in the y axis
W is the normal force per unit length applied to gear
x' and y' are the first derivative of the sine tooth profile position x and y versus the tooth profile angle φ, respectively

x'' and y'' represent the second derivatives of the sine tooth profile position x and y versus the tooth profile angle φ, respectively
x_1 is the position coordinate of any point on the sine tooth profile in x_1 axis direction
y_1 is the position coordinate of any point on the sine tooth profile in y_1 axis direction
x_{k1} and y_{k1} are the coordinates of meshing point K in the coordinate system $\Sigma_1(x_1, o_1, y_1)$
x_{k2} and y_{k2} are the coordinates of meshing point K in the coordinate system $\Sigma_2(x_2, o_2, y_2)$
z_1 is the tooth number of the planet gear
z_2 is the tooth number of the central ring
z_s is the tooth number in mesh
α_i is the pressure angle of the tooth i when multi-teeth are in mesh
α_{k1} is the pressure angle of the gear 1 at the meshing point k
α_{k2} is the pressure angle of the gear 2 at the meshing point k
γ_{50} is the viscosity of lubricating oil
δ is the load proportion coefficient of the bearing on the eccentric shaft
η_0 is the dynamic viscosity of the lubricating oil
η_H is the transmission efficiency of the sinusoidal planetary reducer
η_r is the bearing efficiency on the eccentric shaft section
η_K is the efficiency of the equi-speed output mechanism
η_1 is the efficiency related to the load
η_b is the total rolling bearing efficiency of the reducer
η_{b1} is the total bearing efficiency without eccentricity
η_{b2} is the total bearing efficiency with eccentricity
η_b' is the bearing efficiency on the non-eccentric shaft section
μ_1 and μ_2 is the Poisson's ratio of gear 1 and gear 2 materials, respectively
ζ is the angle between lines o_1K and o_2K
φ is the angle position coordinate of any point on the sine tooth profile
φ_1 is the rotating angle of the planet gear
φ_2 is the rotating angle of the center ring
ω_1 and ω_2 are the angular speeds of the planetary gear and the center ring, respectively

References

[1] H.Y. Ding, Z.Y. Shi, Y.S. Hu, Lightweight design optimization for legs of bipedal humanoid robot, Struct. Multidiscip. Optim. 64 (4) (2021) 2749–2762.
[2] D.S. Carabis, J.T. Wen, Trajectory generation for flexible-joint space manipulators, Frontiers in robotics and AI 9 (2022) 687595.
[3] M. Kamel, The voliro omniorientational hexacopter: an agile and maneuverable tiltable-rotor aerial vehicle, IEEE Robot. Autom. Mag. 25 (4) (2018) 34–44.
[4] D. Sun, N. Wan, W. Dai, Control design for an aerial manipulator for pick-and-place tasks, in: AIAA Scitech 2019 Forum, AIAA, 2019, pp. 1–18.
[5] R.S. Pablo, C.A. Begoña, O. Anibal, Grasp planning and visual servoing for an outdoors aerial dual manipulator, Engineering 6 (2020) 77–88.
[6] X. Meng, Y. He, F. Gu, Design and Implementation of Rotor Aerial Manipulator System, 2016 IEEE International Conference on Robotics and Biomimetics (ROBIO), IEEE., 2016, pp. 673–678.
[7] H. Chen, F. Quan, L. Fang, Aerial grasping with a lightweight manipulator based on multi-objective optimization and visual compensation, Sensors 19 (19) (2019) 42–53.
[8] X.J. Sheng, Z. Ma, N.B. Zhang, Aerial contact manipulation with soft end-effector compliance and inverse kinematic compensation, Journal of Mechanisms and Robotics-Transactions of the ASME. 13 (1) (2021) 011023.
[9] O. Anibal, T. Marco, S. Alejandro, Past, Present and Future of aerial robotic manipulators, IEEE Transactions on Robotics 38 (1) (2022) 626–645.
[10] A. Ollero, The aeroarms project: aerial robots with advanced manipulation capabilities for inspection and maintenance, IEEE Robot. Autom. Mag. 25 (4) (2018) 12–23.
[11] D. Brescianini, R.D. Andrea, Computationally effificient trajectory generation for fully actuated multirotor vehicles, IEEE Trans. Robot. 34 (3) (2018) 555–571.
[12] A. Suarez, G. Heredia, A. Ollero, Design of an anthropomorphic, compliant and lightweight dual arm for aerial manipulation, IEEE Access 6 (2018) 29173–29189.
[13] M. Tognon, B. Yüksel, G. Buondonno, Dynamic decentralized control for protocentric aerial manipulators, in: IEEE International Conference on Robotics and Automation (ICRA), Marina Bay, Singapore, 2017, pp. 6375–6380, 2017.
[14] A. Suarez, G. Heredia, A. Ollero, Design of an anthropomorphic, compliant and lightweight dual arm for aerial manipulation, IEEE Access 6 (2018) 29173–29189.
[15] P. Hannibal, R.M. Ricardo, L. Robert, Lightweight multipurpose three-arm aerial manipulator systems for UAV adaptive leveling after landing and overhead docking, Drones 6 (2022) 380.
[16] I. Nursultan, S. Sumil, K. Dogan, K. Erdal, Design, development and experimental validation of a lightweight dual-arm aerial manipulator with a COG balancing mechanism, Mechatronics 82 (2022) 102–719.
[17] P. Chermprayong, K. Zhang, F. Xiao, An integrated delta manipulator for aerial repair: a new aerial robotic system, IEEE Robot. Autom. Mag. 26 (1) (2019) 54–66.
[18] S. Alejandro, E. Antonio, M. Victor, Design of a lightweight dual arm system for aerial manipulation, Mechatronics 50 (2018) 30–44.
[19] P.E.I. Pounds, D.R. Bersak, A.M. Dollar, Stability of small-scale UAV helicopters and quadrotors with added payload mass under PID control, Auton. Robots. 33 (1/2) (2012) 129–142.
[20] H. Paul, R. Miyazaki, R. Ladig, K. Shimonomura, Landing of a multirotor aerial vehicle on an uneven surface using multiple on-board manipulators, Proc. IEEE/RSJ Int. Conf. Intell. Robots Syst. (2019) 1926–1933.
[21] A. Suarez, G. Heredia, A. Ollero, Design of an anthropomorphic, compliant and lightweight dual arm for aerial manipulation, IEEE Access 6 (2018) 29173–29189.

[22] P. Chermprayong, K. Zhang, F. Xiao, M. Kovac, An integrated delta manipulator for aerial repair: a new aerial robotic system, IEEE Robot. Autom. Mag. 26 (1) (2019) 54–66.
[23] K.K. Lee, S.W. Hong, J.H. Oh, Development of a lightweight and high-efficiency compact cycloidal reducer for legged robots, Int. J. Precis. Eng. Manuf. 21 (3) (2020) 415–425.
[24] Y.H. Yang, G.C. Zhou, L. Chang, G. Chen, A modelling approach for kinematic equivalent mechanism and rotational transmission error of RV reducer, Mech. Mach. Theor. 163 (2021) 104–384.
[25] A.D. Pham, H.J. Ahn, Rigid precision reducers for machining industrial robots, Int. J. Precis. Eng. Manuf. 22 (8) (2021) 1469–1486.
[26] Y.H. Xie, L.X. Xu, Y.Q. Deng, A dynamic approach for evaluating the moment rigidity and rotation precision of a bearing-planetary frame rotor system used in RV reducer, Mechanism and Machine, Theory 173 (2022) 104–851.
[27] D. Vassileva, Y. Kiyosawa, M. Suzuki, Sensorless torque control for a robot with harmonic drive reducers, Mechanice Based Design of Structures and Machines 39 (2) (2011) 253–267.
[28] K.K. Lee, S.W. Hong, J.H. Oh, Development of a lightweight and high-efficiency compact cycloidal reducer for legged robots, Int. J. Precis. Eng. Manuf. 21 (3) (2020) 415–425.
[29] M. Uemura, Y. Mitabe, S. Kawamura, Simultaneous gravity and Gripping force compensation mechanism for lightweight Hand-arm robot with low-reduction reducer, Robotica 37 (6) (2019) 1090–1103.
[30] L. Xu, Z. Fu, Multi-field coupled dynamics for a movable tooth drive system integrated with shape memory alloys, Heliyon 9 (7) (2023) e17531.
[31] L. Mizzi, S. Hoseini, M. Formighieri, et al., Development and prototyping of SMA-metamaterial biaxial composite actuators, Smart Mater. Struct. 32 (3) (2023) 035027.
[32] J. Jungblut, J. Haas, S. Rinderknecht, A new active balancing device utilizing rotating piezo actuators, Mech. Syst. Signal Process. 181 (2022) 109521.
[33] T. Ozaki, N. Ohta, Power-efficient driver circuit for piezo electric actuator with passive charge recovery, Energies 13 (11) (2020) 2866.
[34] G. Novelli, G. Vargas, R. Andrade, Dielectric elastomer actuators as artificial muscles for wearable robots, J. Intell. Mater. Syst. Struct. 34 (9) (2023) 1007–1025.
[35] L. Xu, J. Yan, A double-stage movable tooth reducer with cam wave generator, J. Braz. Soc. Mech. Sci. Eng. 45 (3) (2023) 165.
[36] F. Litvin, Gear Geometry and Applied Theory, Publisher: Cambridge University Press, 1994.
[37] B.W. Kelley, A.J. Lemanski, Lubrication of involute gearing 182 (31) (1967) 173–184.
[38] X. Hai, Development of a Generalized Mechanical Efficiency Prediction Methodology for Gear Pairs, D. The Ohio State University, 2005, pp. 102–107.
[39] L. Xu, Y. Yang, Friction Design of Mechanical Parts, China Machinery Industry Press, Beijing, 1998.